



1 Erosion rates in a wet, temperate climate derived from rock 2 luminescence techniques 3

4 Rachel K. Smedley¹, David Small², Richard S. Jones^{2,3}, Stephen Brough¹, Jennifer Bradley¹, Geraint T.H. Jenkins⁴

5 ¹ School of Environmental Sciences, University of Liverpool, Liverpool, UK.

6 ² Department of Geography, Durham University, South Road, Durham, UK.

7 ³ School of Earth, Atmosphere and Environment, Monash University, Melbourne, Australia.

8 ⁴ Independent researcher: Powys, Wales, UK

9 *Correspondence to:* Rachel K. Smedley (rachel.smedley@liverpool.ac.uk)

10 Abstract

11 A new luminescence erosion-meter has huge potential for inferring erosion rates on sub-millennial scales for both steady and
12 transient states of erosion, which is currently not possible with any existing techniques capable of measuring erosion. This
13 study applies new rock luminescence techniques to a well-constrained scenario provided by the Beinn Alligin rock avalanche,
14 NW Scotland. Boulders in this deposit are lithologically consistent, have known cosmogenic nuclide ages, and independently-
15 derived Holocene erosion rates. We find that luminescence-derived exposure ages for the Beinn Alligin rock avalanche were
16 an order of magnitude younger than existing cosmogenic nuclide exposure ages, suggestive of high erosion rates (as supported
17 by field evidence of quartz grain protrusions on the rock surfaces). Erosion rates determined by luminescence were consistent
18 with independently-derived rates measured from boulder-edge roundness. Inversion modelling indicates a transient state of
19 erosion reflecting the stochastic nature of erosional processes over the last ~4 ka in the wet, temperate climate of NW Scotland.
20 Erosion was likely modulated by known fluctuations in moisture availability, and to a lesser extent temperature, which
21 controlled the extent of chemical weathering of these highly-lithified rocks prior to erosion. The use of a multi-elevated
22 temperature, post-infra-red, infra-red stimulated luminescence (MET-pIRIR) protocol (50, 150 and 225°C) was advantageous
23 as it identified samples with complexities introduced by within-sample variability (e.g. surficial coatings). This study
24 demonstrates that the luminescence erosion-meter can infer accurate erosion rates on sub-millennial scales and identify
25 transient states of erosion (i.e. stochastic processes) in agreement with independently-derived erosion rates for the same
26 deposit.

28 1. Introduction

29 Rock erosion is dependent upon a variety of internal (e.g. mineralogy, grain size, porosity, structures) and external (e.g.
30 temperature, moisture availability, snow cover, wind, aspect) factors. Chemical and/or physical weathering of rocks (or rock



31 decay; Hall et al. 2012) breaks down the surficial materials making them available for transportation (i.e. erosion), where the
32 rates and processes of degradation is primarily controlled by the rock lithology (e.g. Twidale, 1982; Ford and Williams, 1989).
33 For boulders with similar lithologies, the erosion rate is conditioned by weathering principally caused by moisture availability,
34 but also temperature, and in some cases biological factors (Hall et al. 2012). It is widely reported that warmer temperatures
35 increase most rates of chemical activity, while sub-zero temperatures arrest chemical activity on a seasonal basis. However,
36 cold temperatures alone do not preclude chemical weathering (Thorn et al. 2001). As such, rock erosion rates will be sensitive
37 to changing climate (moisture availability, temperature) such as that experienced throughout the Late Holocene (i.e. last 4 ka)
38 (e.g. Charman, 2010), in addition to that forecast for the future due to anthropogenic climate change (e.g. Stocker et al. 2013).
39 Measuring erosion rates over shorter ($\leq 10^3$ a) and longer ($\geq 10^4$ a) integration times is advantageous as each targets a different
40 phenomenon of erosion. Longer timeframes will inform on how landscapes respond to changing large-scale climatic and
41 tectonic conditions (e.g. Herman et al. 2010), whereas shorter timeframes assess local or regional responses to shorter-lived
42 environmental conditions (e.g. climate fluctuations). A number of techniques can constrain long-term, landscape erosion rates
43 on $\geq 10^4$ a timeframes, such as cosmogenic nuclides (e.g. Lal, 1991; Braun et al. 2006; Balco et al. 2008) or thermochronology
44 (Reiners and Brandon, 2006). While observational measurements on very short timeframes $\leq 10^2$ a are performed with both
45 direct contact (e.g. Hanna, 1966; High and Hanna, 1970; Trudgill et al. 1989) and non-contact (e.g. Swantesson, 1989;
46 Swantesson et al. 2006) techniques. However, until now it has been difficult to constrain rates on 10^2 to 10^3 a timeframes due
47 to a lack of techniques with the required sensitivity and resolution.

48 The luminescence signal within mineral grains (quartz and feldspar) is reset when a rock surface is exposed to sunlight
49 for the first time (e.g. Habermann et al. 2000; Polikreti et al. 2002; Vafiadou et al. 2007). With continued exposure the
50 luminescence signal resetting in the mineral grains propagates to increasing depths (i.e. the luminescence depth profile is a
51 function of time). Improved understanding of this fundamental principle has led to the development of new applications of
52 luminescence; constraining the timing of rock exposure events (Laskaris and Liritzis, 2011; Sohbaty et al. 2011; Lehmann et
53 al. 2018) and rock surface erosion rates (Sohbaty et al. 2018; Lehmann et al. 2019a,b). Here, we measure erosion rates, rather
54 than weathering rates as the luminescence technique specifically measures the light penetration into a rock surface after the
55 removal of material (i.e. erosion), occurring after the in-situ rock breakdown (i.e. weathering). Luminescence depth profiles
56 are a product of the competing effects of time (which allows the bleaching front to propagate to greater depths) and erosion
57 (which exhumes the bleaching front closer to the surface). Existing studies have suggested that rock luminescence exposure
58 dating is only feasible for very short timeframes (e.g. < 300 a; Sohbaty et al. 2018) as light penetrates faster than the material
59 can be removed, and/or in settings where erosion rates are < 1 mm/ka (Lehmann et al. 2018). Beyond this, the dominant control
60 on the luminescence depth profile is erosion, rather than time, hence if time can be parameterised, then erosion can be
61 determined (and vice versa).

62 New luminescence techniques have the potential to derive 10^2 to 10^3 a scale erosion rates because of two important
63 characteristics: (1) measurable luminescence depth profiles can develop in a rock surface over extremely short durations of



64 sunlight exposure (e.g. days; Polikreti et al. 2003, or years; Lehmann et al. 2018); and (2) luminescence depth profiles are
65 sensitive to mm-scale erosion. Conversely cosmogenic nuclides are sensitive to m-scale erosion, depending on the density (e.g.
66 Lal, 1991). Therefore, the new luminescence erosion-meter has the potential to provide a step-change in capabilities of
67 measuring erosion rates on currently impossible 10^2 to 10^3 a timeframes. However, its application has been limited to few
68 studies (e.g. Sohbati et al. 2018; Lehmann et al. 2019b) validated against long-term erosion rates of landscape evolution from
69 global or regional datasets rather than local, independently-constrained erosion rates derived from the same rock type.

70 This study tests the accuracy and applicability of rock erosion rates inferred from luminescence techniques in a new
71 latitudinal (57°N) and climate (wet, temperate) setting with independently-constrained erosion rates. The Beinn Alligin rock
72 avalanche in NW Scotland (Fig. 1) provides a well-constrained test scenario as: (1) the boulders were sourced from a single
73 fault-bounded failure scarp occurring within sandstones of the Torridonian group (i.e. rocks are likely to be lithologically
74 consistent); (2) all boulder samples share an identical exposure history as they were deposited by a single, instantaneous event;
75 (3) independent cosmogenic exposure ages constrain the timing of the rock avalanche (Ballantyne and Stone, 2004); and (4)
76 independently-derived erosion rates over the last ~ 4 ka for the boulders of the Beinn Alligin rock avalanche uniquely provide
77 constraints on erosion rates (Kirkbride and Bell, 2010).

78 2. Theoretical background

79 The propagation of a bleaching front (i.e. the depth at which the luminescence signal has been reduced by 50 %) into a rock
80 surface can be described by a double exponential function (Eq. 1), where L_x is the luminescence measured with depth (x) from
81 the rock surface, L_0 is the saturation limit for this sample (determined experimentally), t is the exposure time, $\overline{\sigma\varphi_0}$ is the
82 intensity of light of a specific wavelength at the rock surface, and μ is the light attenuation coefficient. To determine the
83 exposure time (t) of a rock surface, it is necessary to parameterise μ and $\overline{\sigma\varphi_0}$, which are likely unique to any specific rock
84 lithology and natural sunlight conditions (e.g. latitude, cloudiness) of the sample being dated, respectively. Therefore, to
85 provide accurate luminescence exposure ages or erosion rates, μ and $\overline{\sigma\varphi_0}$ must be calibrated using samples of known-age with
86 the same lithology and natural sunlight conditions (e.g. a nearby road-cutting).

$$87 \quad L_x = L_0 e^{-\overline{\sigma\varphi_0} t} e^{-\mu x} \quad (1)$$

88 Studies have applied rock luminescence techniques (mostly exposure dating) to a variety of lithologies including granites,
89 gneisses (Lehmann et al. 2018 2019a,b; Meyer et al. 2019), sandstones (Sohbati et al. 2012; Chapot et al. 2012; Pederson et
90 al. 2014) and quartzites (Glignac et al. 2019). These studies showed that μ is highly dependent upon the rock lithology, where
91 mineralogy has a strong control on the rock transparency. This is supported by direct measurements of μ for a variety of
92 lithologies (greywacke, sandstone, granite, and quartzite) using a spectrometer (Ou et al. 2018). In addition to mineralogy, it
93 has also been shown that the precipitation of dark Fe-hydroxides (Meyer et al. 2018) and rock varnishing (or weathering crusts)
94 (e.g. Luo et al. 2019) can influence μ by changing the rock transparency principally at the rock surface. Mineralogy is broadly
95 a constant variable over time. However, the formation of precipitates or rock varnishing can be time-variable due to changing
96 environmental factors external to the rock; thus, we must consider the possibility that μ may be time-variable. Consequently,



97 investigating the rock opacity of each sample is important to assess whether the known-age samples used to parameterise μ
98 and $\overline{\sigma\varphi_0}$ were consistent with the unknown-age samples used for exposure dating or erosion rates.

99 Since the introduction of the new rock luminescence techniques, most studies on K-feldspar (except Luo et al. 2019)
100 have only utilised the IR₅₀ signal as it bleaches more efficiently with depth into rock surfaces compared to higher temperature
101 post-IR IRSL signals (e.g. Luo et al. 2019; Ou et al. 2018). However, electron multiplying charged coupled device (EMCCD)
102 measurements of four rock types (quartzite, orthoclase and two different granites) have shown that the post-IR IRSL signals
103 of rock slices were dominated by K-feldspars, while Na-rich feldspars can contribute towards the IR₅₀ signal (Thomsen et al.
104 2018). It is possible that the different IRSL signals will have different luminescence characteristics (e.g. bleaching rates, fading
105 rates, saturation levels, light attenuation, internal mineral composition) that could be exploited during measurements. Luo et
106 al. (2019) used the post-IR IRSL signals with a multiple elevated temperature (MET) protocol (50, 110, 170, 225 °C) to
107 demonstrate that all the IRSL signals provide luminescence depth profiles, but the lower temperature signals penetrated further
108 into the rock with depth. The authors fit the four IRSL signals to improve the accuracy of their parameterisation of μ and $\overline{\sigma\varphi_0}$.
109 However, no study has yet used the MET-post IR IRSL protocol to exploit the differing luminescence characteristics of the
110 simultaneously-measured IRSL signals to provide an internal quality control check on the reliability of the measured data, i.e.
111 the luminescence depth profile will penetrate deeper in to the rock for the IR₅₀ signal than the pIRIR₁₅₀ signal, which in turn
112 will penetrate deeper than the pIRIR₂₂₅ signal. However, all three signals should determine the same erosion rates if the model
113 parameterisation (i.e. μ and $\overline{\sigma\varphi_0}$) is accurate. To maximise the potential information that could be derived from the samples,
114 this study applied a MET-post IR IRSL protocol (50, 150 and 225 °C).

115 For determining erosion rates for rock surfaces of known exposure age, Sohbaty et al. (2018) use a confluent
116 hypergeometric function to provide an analytical solution, but assuming only steady-state erosion. Lehmann et al. (2019a)
117 provide a numerical approach that exploits the differential sensitivities to erosion of the luminescence (short-term) and
118 cosmogenic nuclide (longer-term) techniques to erosion to infer erosion histories (steady state and transient over time) for rock
119 surfaces. By applying a step function from zero to increased constant erosion rates at certain times in history, this numerical
120 approach (Lehmann et al. 2019a) allows erosion history to be considered as non-constant in time (i.e. transient), in addition to
121 steady-state, and so it is more indicative of the stochastic erosional processes (driven by temperature, precipitation, snow cover,
122 wind) in nature.

123 3. The Beinn Alligin rock avalanche

124 Today, average winter and summer temperatures in NW Scotland are 7°C and 18°C, respectively, while average annual
125 precipitation (mostly rainfall) is high (ca. 2,300 mm/a) (Met Office, 2021). The Beinn Alligin rock avalanche (57°35'N,
126 05°34'W) is a distinct, lobate deposit of large boulders that is 1.25 km long and covers an area of 0.38 km². It has previously
127 been ascribed various origins including a rockslide onto a former corrie glacier (e.g. Ballantyne, 1987; Gordon, 1993) and a
128 former rock glacier (Sissons, 1975; 1976). However, on the basis of cosmogenic exposure dates that constrain its deposition
129 to the Middle to Late Holocene it is now widely accepted to have been deposited by a rock-slope failure that experienced



130 excess run-out (e.g. a rock avalanche). The source is a distinct, fault-bounded failure scar on the southern flank of Sgurr Mor,
131 the highest peak of Beinn Alligin (Ballantyne, 2003; Ballantyne and Stone, 2004). The rock avalanche is comprised of large,
132 poorly-sorted boulders and is calculated to comprise a total volume of $3.3 - 3.8 \times 10^6 \text{ m}^3$, equivalent to a mass of 8.3 – 9.5 Mt
133 (Ballantyne and Stone, 2004). The source lithology is Late Precambrian Torridonian sandstone strata. The Torridonian
134 sandstones are reddish or reddish brown terrestrial sedimentary rocks deposited under fluvial or shallow lake conditions
135 (Stewart, 1982). The sandstones maintained a common origin throughout deposition (Stewart, 1982) and are thus largely
136 consistent in mineralogy (dominated by quartz and alkali and plagioclase feldspar) although there are some local variations in
137 grain size (Stewart and Donnellan, 1992).

138 The ^{10}Be concentrations of three boulders used for cosmogenic nuclide exposure dating were internally consistent
139 evidencing a single, catastrophic mass movement event which occurred $4.22 \pm 0.34 \text{ ka}$ (re-calculated from Ballantyne and
140 Stone, 2004). Consequently, the boulders were very unlikely to have previously been exposed to cosmic rays or sunlight prior
141 to transport and deposition. Moreover, the large size of the flat-topped boulders ($>2 \times 2 \times 2 \text{ m}$) and lack of finer sediment
142 matrix within the rock avalanche deposit, suggested that post-depositional movement or exhumation is unlikely. The
143 Torridonian sandstones are hard, cemented rocks (Stewart, 1984; Stewart and Donnellson, 1992) susceptible to granular
144 disintegration (e.g. Ballantyne and Whittington, 1987). Given its location salt weathering is likely negligible. Kirkbride and
145 Bell (2010) estimated edge-rounding rates of $\sim 3.3 \text{ mm/ka}$ for a suite of Torridonian sandstone boulder samples from a range
146 of sites in NW Scotland under the warmer, wetter climates of the Holocene. A notably higher erosion rate of 12 mm/ka was
147 specifically determined for the Beinn Alligin rock avalanche. Kirkbride and Bell (2010) suggest that this higher erosion rate,
148 in comparison to the other sites, is likely due to inherited rock roundness caused by abrasion during the high-magnitude
149 depositional event. Additionally, minor differences in lithology cannot be ruled out (e.g. Twidale, 1982; Ford and Williams,
150 1989). Consequently, we consider the range ~ 3.3 to 12 mm/ka as a reasonable estimation of the Holocene erosion rate of the
151 Torridonian sandstone boulders that comprise the Beinn Alligin rock avalanche.

152 **4. Methods**

153 A total of six rock samples were taken from the Torridonian sandstones in NW Scotland (Fig. 2). Three samples were taken
154 from three different road-cuttings of known age to calibrate values of μ and $\overline{\sigma\phi_0}$: ROAD01 (0.01 a), ROAD02 (57 a), ROAD03
155 (44 a). Three further samples were taken from flat-topped, angular boulders that were part of the Beinn Alligin rock avalanche
156 deposit: BALL01, BALL02 and BALL03. Samples were collected in daylight and immediately placed into opaque, black
157 sample bags. All samples were taken from surfaces perpendicular to incoming sunlight to ensure that the daylight irradiation
158 geometry was similar between calibration and dating samples (cf. Gliganic et al. 2019).

159 *4.1 Luminescence measurements*

160 To calculate the environmental dose-rate throughout burial for each sample (Table 1), U, Th and K concentrations were
161 measured for ca. 80 g of crushed bulk sample using high-resolution gamma spectrometry. Internal dose-rates were calculated
162 using measured average grain sizes for each sample. Cosmic dose-rates were calculated after Prescott and Hutton (1994). For



163 measuring the luminescence depth profiles, sample preparation was performed under subdued-red lighting conditions to
164 prevent contamination of the luminescence signal. Rock cores ~7 mm in diameter and up to 20 mm long were drilled into the
165 rock surface using an Axminster bench-top, pillar drill equipped with a water-cooled, diamond-tipped drillbit (~9 mm
166 diameter). Each core was sliced at a thickness of ~0.7 mm using a Buehler IsoMet low-speed saw equipped with a water-
167 cooled, 0.3 mm diameter diamond-tipped wafer blade. All slices were then mounted in stainless steel cups for luminescence
168 measurements.

169 Luminescence measurements were performed on a Risø TL/OSL reader (TL-DA-15) with a $^{90}\text{Sr}/^{90}\text{Y}$ beta irradiation
170 source. Heating was performed at $1^\circ\text{C}/\text{s}$ and the rock slices were held at the stimulation temperature (i.e. 50, 150 and 225°C)
171 for 60 s prior to IR stimulation to ensure all of the disc was at temperature before stimulating (cf. Jenkins et al. 2018). IRSL
172 signals were detected in blue wavelengths using a photo-multiplier tube fitted with Schott BG-39 (2 mm thickness) and Corning
173 7-59 (2 mm thickness) filters. A MET-post-IR IRSL sequence (Table S1) was used to determine IRSL signals at three different
174 temperatures (50, 150 and 225°C) simultaneously, hereafter termed the IR_{50} , pIRIR_{150} and pIRIR_{225} signals. OSL depth profiles
175 were determined for each core by measuring the natural signal (L_n) normalised using the signal measured in response to a 53
176 Gy test-dose (T_n), hereafter termed the L_n/T_n signal. The IRSL signal was determined by subtracting the background signal
177 (final 20 s, 40 channels) from the initial signal (0 – 3.5 s, 7 channels). The large test-dose (53 Gy) was used to reduce the
178 impact of thermal transfer/incomplete resetting of the IRSL signal between measurements (after Liu et al. 2016).

179 D_e values were determined for the shallowest disc and the deepest disc from one core of each sample to quantify the
180 natural residual dose and saturation limit (L_0 , Eq. 1), respectively. Fading rates (g -values, Aitken 1985) were determined for
181 three discs of each sample and normalised to a t_c of two days (Huntley and Lamothé 2001). The weighted mean and standard
182 error of the g -values for all discs were $3.7 \pm 0.4 \text{ \%/dec.}$ (IR_{50}), $1.0 \pm 0.5 \text{ \%/dec.}$ (pIRIR_{150}) and $1.0 \pm 0.5 \text{ \%/dec.}$ (pIRIR_{225}).
183 The large uncertainties on the individual g -values measured were derived from uncertainty in the fit of the data, which is
184 typical of fading measurements (e.g. Smedley et al. 2016). The fading rates were in line with previous IRSL signals (e.g.
185 Roberts 2012; Trauerstein et al. 2014; Kolb and Fuchs 2018). Lehmann et al. (2019a) performed sensitivity tests of the shape
186 of the luminescence depth profiles (IR_{50}) with a high and low g -value end-members and these simulations demonstrated that
187 athermal loss of signal has a minimal impact upon the IRSL depth profile shape; thus, athermal loss (i.e. fading rates) was not
188 considered in calculations.

189 Previous studies have shown that the IR_{50} signal bleached faster than the pIRIR signals (Smedley et al., 2015). To test
190 the inherent bleaching rates of the feldspars in our samples, artificial bleaching experiments were performed on seven discs
191 from all six samples (n.b. these experiments do not test for variations in light attenuation with depth). All previously-analysed
192 discs were given a 105 Gy dose, then subjected to different exposure times in a solar simulator (0 m, 1 m, 10 m, 30 m, 1 h, 4
193 h and 8 h) and the normalised luminescence signals (IR_{50} , pIRIR_{150} and pIRIR_{225}) were measured (Fig. S1). The results show
194 some variations after 1 m of solar simulator exposure. However, luminescence signals reduced to 2 – 6 % (IR_{50}), 6 – 11 %
195 (pIRIR_{150}) and 14 – 22 % (pIRIR_{225}) of the unexposed light levels after 1 h and 1 – 2 % (IR_{50}), 2 – 3 % (pIRIR_{150}) and 4 – 7 %



196 (pIRIR₂₂₅) after 8 h. This indicates that within our samples the minerals emitting the IRSL signals (i.e. K-feldspar) have similar
197 inherent bleaching rates.

198 4.2 *Rock composition*

199 After luminescence measurements were performed, each rock slice was analysed to investigate potential changes in rock
200 composition with depth (inferred by opacity). The average down-core grainsize of each sample was measured under an optical
201 microscope. Down-core red-green-blue (RGB) values were determined for each sample to investigate whether there was any
202 colour variation within the sample, and externally between samples; thus, providing a semi-quantitative tool to detect
203 variability in rock opacity (Meyer et al. 2018). Raster images of RGB were obtained for each rock slice using an EPSON
204 Expression 11000XL flatbed scanner at 1200 dpi resolution (e.g. Fig. S2). Mean and standard deviations of the RGB values
205 (e.g. Fig. 3) for each rock slice were calculated using the *raster* package in R (version 2.9-23; Hijmans, 2019).

206 5. Results

207 5.1 Luminescence depth profiles

208 The luminescence depth profiles (IR₅₀, pIRIR₁₅₀ and pIRIR₂₂₅) (Fig. 4) record bleaching fronts caused by sunlight exposure
209 for all of the known-age samples. The luminescence depth profile measured for core 3 of sample ROAD02 (Fig. 4 g,h,j) was
210 inconsistent with cores 1 and 2, giving high standard deviation values for the IR₅₀ (1.2), pIRIR₁₅₀ (1.1) and pIRIR₂₂₅ (0.9)
211 signals; thus, core 3 was removed from subsequent analysis (likely sample preparation issues related to drilling preservation).
212 The luminescence depth profiles for the remaining replicate cores for all three samples were broadly consistent within each
213 rock sample with mean standard deviations ranging from 0.2 – 0.8.

214 The luminescence depth profiles (Fig. 4) for the IR₅₀ signal were consistent with the increasing sunlight exposure
215 ages for ROAD01 (0.01 a), ROAD03 (44 a) and ROAD02 (57 a), with bleaching fronts at 2.5 mm, 4.5 mm and 6.5 mm,
216 respectively (Fig. S4a). This indicated that the depth of the IR₅₀ bleaching front was dominated by exposure duration for the
217 known-age samples as expected. Similarly, the pIRIR₁₅₀ and pIRIR₂₂₅ bleaching fronts were shallower in sample ROAD01
218 (1.5 mm) compared to ROAD02 and ROAD03 (2.5 – 3.5 mm), reflecting the younger exposure duration of ROAD01.
219 However, the pIRIR₁₅₀ and pIRIR₂₂₅ bleaching fronts were at similar depths (3.5 mm and 2.5 mm respectively) for both
220 ROAD02 (57 a) and ROAD03 (44 a). This suggests that either another factor is influencing light penetration with depth in
221 these rocks or that the pIRIR signals cannot resolve between a 57 a and 44 a exposure history (difference of only 13 a).

222 The luminescence depth profiles measured for the unknown-age samples BALL02 and BALL03 using the IR₅₀,
223 pIRIR₁₅₀ and pIRIR₂₂₅ signals (Fig. 5) recorded bleaching fronts caused by sunlight exposure. Conversely, the luminescence
224 depth profile for sample BALL01 had saturated IRSL signals throughout the core and did not display any evidence of IRSL
225 signal resetting with depth (Fig. 5a-c). A luminescence depth profile measured for a core drilled into the bottom surface
226 (Bottom C1; Fig. 5a-c) confirmed that the bottom surface of BALL01 was also saturated. The lack of a bleaching front in
227 sample BALL01 is difficult to explain as the sample was taken in daylight and had seemingly identical characteristics to
228 samples BALL02 and BALL03 (i.e. no lichen-cover or coatings preventing light penetration in the rock). Although all the



229 samples were similar in colour/opacity (Fig. 3a), sample BALL01 was coarser grained than BALL02 and BALL03 (Fig. 2;
230 Fig. 3b). Studies have shown that coarser grain sizes are more susceptible to mechanical weathering via grain detachment
231 induced by chemical weathering (Israeli and Emmanuel, 2018); thus, although care was taken, it is possible that the
232 luminescence depth profile (likely <10 mm based on BALL02 and BALL03) was lost during sampling and/or sample
233 preparation due to the presence of a fragile weathering crust, potentially with a sub-surface zone of weakness (e.g. Robinson
234 and Williams, 1987). Furthermore, field observations showed the presence of a rock pool on the surface of the boulder sampled
235 for BALL01 (Fig. 1a), which is not present on BALL02 (Fig. 1b) and BALL03 (Fig. 1c); thus, there is also potential that the
236 surface sampled for BALL01 had experienced enhanced chemical weathering via trickle paths draining the rock pool. These
237 are commonly linked to a greater density of micro-cracks in the uppermost mm's of the rock (Swantesson, 1989, 1992).
238 Consequently, we did not derive exposure ages or erosion rates from BALL01. Where rock pools are likely on boulders, the
239 highest rock surface should be sampled for luminescence techniques to avoid the potential for pooling or trickle paths.

240 5.2 Estimation of model parameters

241 To determine an apparent exposure age or erosion rate from the measured luminescence depth profiles, the variables that
242 control the evolution of a luminescence depth profile in a rock surface must be parameterised; specifically, the dose-rate (\dot{D})
243 (see Section 4.1), saturation level (D_0), $\overline{\sigma\varphi_0}$ and μ . D_0 was determined experimentally from saturated dose-response curves
244 measured for the deepest rock slices of each sample. $\overline{\sigma\varphi_0}$ and μ were calibrated using the known-age samples of similar,
245 suitable rock composition as determined by the down-core profiles of RGB and grainsize (Section 4.2). Down-core RGB
246 values for all samples were internally consistent (Fig. 3a) as indicated by the relative standard deviation (RSD) range between
247 8 and 12 %. The down-core RGB values were also externally consistent between all samples (Fig. 3a), with the exception of
248 the slightly darker-coloured sample ROAD01. However, measurements of grainsize (Fig. 3b) showed that the known-age
249 sample ROAD02 ($90 \pm 23 \mu\text{m}$) had a similar grainsize to the unknown-age samples BALL02 ($73 \pm 18 \mu\text{m}$) and BALL03 (98
250 $\pm 19 \mu\text{m}$), whereas ROAD01 ($42 \pm 9 \mu\text{m}$) and ROAD03 ($168 \pm 56 \mu\text{m}$) were finer and coarser grained, respectively. Given the
251 similarity in colour and grain size, it was considered most appropriate to calibrate $\overline{\sigma\varphi_0}$ and μ for the unknown age samples
252 (BALL02 and BALL03) using known-age sample ROAD02.

253 The values of $\overline{\sigma\varphi_0}$ and μ were determined by fitting Eqn. (1) using the approach of Lehmann et al. (2019). The
254 inferred model (Eq. 1) had a good fit to the measured data for all samples and signals (Fig. 4) and μ and $\overline{\sigma\varphi_0}$ were calculated
255 (Table 2; Fig. 6). The μ values for samples ROAD01, ROAD02 and ROAD03 determined using the IR₅₀ signal in this study
256 were comparable to μ values in existing literature for sandstones e.g. $\mu = 1.01 \text{ mm}^{-1}$ where $\overline{\sigma\varphi_0} = 6.80\text{e}^{-9} \text{ s}^{-1}$ (Sohbati et al.
257 2012) and 3.06 mm^{-1} (Ou et al. 2018). For sample ROAD01, μ and $\overline{\sigma\varphi_0}$ were similar for all three IRSL signals with large
258 uncertainties (Fig. 6a-c) which is likely related to the shorter exposure age of this sample (0.01 a). The finer grain size and
259 darker rock opacity of sample ROAD01 in comparison to ROAD02 and ROAD03 likely explained the larger values of μ (i.e.
260 greater light attenuation with depth into the rock surface).

261 5.3 Apparent exposure ages and erosion rates



262 Luminescence exposure ages were determined from the luminescence depth profiles using μ and $\overline{\sigma\phi_0}$ derived from sample
263 ROAD02 for each of the IRSL signals (Table 3). For BALL03, the IR_{50} ($378 \pm 115 \text{ a}^{-1}$), $pIRIR_{150}$ ($294 \pm 61 \text{ a}^{-1}$) and $pIRIR_{225}$
264 ($370 \pm 46 \text{ a}^{-1}$) signals all gave luminescence exposure ages in agreement within uncertainties. For BALL02, the three signals
265 were inconsistent with one another. The $pIRIR_{225}$ signal ($279 \pm 48 \text{ a}^{-1}$) was consistent with BALL03, but the IR_{50} ($9 \pm 3 \text{ a}^{-1}$)
266 and $pIRIR_{150}$ ($70 \pm 9 \text{ a}^{-1}$) signals for BALL02 were younger than BALL03. All apparent exposure ages based on the different
267 luminescence signals were at least one order of magnitude younger than the apparent exposure age based cosmogenic nuclide
268 dating ($4.22 \pm 0.34 \text{ ka}$; Ballantyne and Stone, 2004). This was likely because erosion over time in this wet, temperate climate
269 has removed material from the surface of the rock and created shallower luminescence depth profiles; thus, the luminescence
270 depth profile is dependent upon both exposure age and the erosion rate (Sohbati et al. 2018; Lehmann et al. 2019a).

271 To test whether erosion rates could be determined for the Beinn Alligin boulders from the luminescence depth
272 profiles, we performed erosion rate modelling following the inversion approach of Lehmann et al. (2019) and constrained by
273 the re-calculated cosmogenic nuclide age (Ballantyne and Stone, 2004). This approach defines an erosion history that follows
274 a step function with an initial period of zero erosion, followed by an immediate increase to a constant erosion rate at a defined
275 time. It attempts to recover parameter combinations (erosion rate and timing of erosion initiation) that are both consistent with
276 the cosmogenic nuclide concentration and produce modelled luminescence profiles that match observations. For sample
277 BALL02, both the IR_{50} and $pIRIR_{150}$ signals suggested that the system had approached a steady-state with erosion rates of 66
278 mm/ka (IR_{50}) and 9 mm/ka ($pIRIR_{150}$) applied over time periods $>73 \text{ a}$ and 593 a, respectively. However, the $pIRIR_{225}$ signal
279 suggested a transient erosion state, where the luminescence signal could be derived from numerous pairs of erosion rates and
280 initiation times. All three IRSL signals from sample BALL03 consistently suggested a system undergoing a transient response
281 to erosion, which was consistent with the $pIRIR_{225}$ signal of BALL02 (Fig. 7, Table 3).

282 6. Discussion

283 6.1 Luminescence depth profiles at Beinn Alligin rock avalanche

284 Despite the similarity in rock opacity, grain size, aspect and exposure history, the luminescence depth profiles for samples
285 BALL02 and BALL03 from the Beinn Alligin rock avalanche were inconsistent (Fig. 5). We consider it unlikely that this lack
286 of consistency was caused by local variations in erosion rates (e.g. due to microclimate, aspect etc; Hall et al. 2005, 2008) as
287 there were discrepancies between all three IRSL signals of BALL02. We would expect local erosion rate variations between
288 samples to be consistently recorded across each of the IRSL signals, assuming the model parameterisation (μ and $\overline{\sigma\phi_0}$) were
289 accurate. Specifically, and with all other things being equal, a locally-variable erosion rate would translate the bleaching
290 front(s) closer to the rock surface by a proportionally consistent amount for each signal of a given sample.

291 Analysis of the rock opacity with depth (Section 4.2; Meyer et al. 2018) showed that sample BALL02 was more
292 positively skewed towards darker colours than ROAD02 and BALL03 (Fig. S2, S3), with higher surficial values caused by
293 Fe-staining. Fe-staining can occur on rock surfaces with seasonal rock pools and trickle paths (Swantesson, 1989, 1992). The
294 presence of a thin Fe-coating ($<1 \text{ mm}$) on the rock surface would have changed the intensity and wavelength of the net daylight



295 flux received by individual grains (e.g. Singhvi et al., 1986; Parish, 1994) and likely increased light attenuation with depth (e.g.
296 Meyer et al. 2018; Luo et al. 2018). Consequently, the parameterisation of μ and $\overline{\sigma\phi_0}$ derived from sample ROAD02 would
297 be inaccurate for BALL02. Interestingly, the similarity between BALL02 and BALL03 for the pIRIR₂₂₅ signal suggests that
298 the presence of an Fe-coating may have preferentially attenuated the wavelengths that influence the IR₅₀ and pIRIR₁₅₀ signals,
299 and not the pIRIR₂₂₅ signal, but this requires further investigation. The application of the MET-pIRIR rather than just the stand-
300 alone IR₅₀ signal protocol provided a major advantage as it identified samples where the parameterisation of μ and $\overline{\sigma\phi_0}$ from
301 known-age samples was complicated by factors such as surficial weathering coatings.

302 The boulders from the Beinn Alligin rock avalanche have been subject to a temperate climate for the last ~4 ka. The
303 luminescence depth profiles from the boulders demonstrated that on these timeframes and under these climatic conditions the
304 technique was an erosion-meter, rather than a chronometer, as expected (Sohbati et al. 2018; Lehmann et al. 2019a). Lehmann
305 et al. (2018) noted that two of their samples, uncorrected for erosion, gave apparent luminescence exposure ages of ca. 640 a
306 and <1 a compared to apparent TCN ages of ca. 16.5 ka and 6.5 ka, respectively. It has thus been inferred that erosion rates >1
307 mm/ka can make interpretation of luminescence depth profiles in terms of an exposure age difficult without accurately
308 constraining the erosion rate (Sohbati et al., 2018; Lehmann et al., 2018). This is consistent with the underestimation of
309 luminescence exposure ages measured here for the Beinn Alligin rock avalanche (Table 3), which have been independently-
310 dated to 4.22 ± 0.34 ka using cosmogenic nuclides (Ballantyne and Stone, 2004). Consequently, luminescence depth profiles
311 for the Beinn Alligin rock avalanche can only be inferred in terms of erosion rates.

312 6.2 Luminescence as an erosion-meter

313 The numerical approach of Lehmann et al. (2019a) exploits the different sensitivities of the luminescence (short-term) and
314 cosmogenic nuclide (longer-term) techniques to erosion to infer erosion histories (steady state and transient over time) for rock
315 surfaces. Their modelling shows that the higher erosion rates (>100 mm/ka) can only be sustained over shorter time durations
316 (up to decadal) while at the same time being consistent with cosmogenic nuclide measurements. For BALL03, transient erosion
317 rates were derived using the IR₅₀ (6 - 460 mm/ka), pIRIR₁₅₀ (14 - 100 mm/ka) and pIRIR₂₂₅ (11 - 180 mm/ka) signals. These
318 modelled transient erosion rates were broadly comparable to erosion rates inferred from luminescence depth profiles over
319 comparable timeframes in previous studies: (i) rates between $<0.038 \pm 0.002$ and 1.72 ± 0.04 mm/ka for glacial boulders and
320 landslides (granite gneiss, granodiorite and quartzite) in the Eastern Pamirs, China (Sohbati et al. 2018); and (ii) between $3.5 \pm$
321 1.2 mm/ka and $4,300 \pm 600$ mm/ka for glacially-modified, granitic bedrock in the French Alps (Lehmann et al., 2019b). This
322 latter study modelled higher erosion rates (>100 mm/ka) over timescales from 10^1 to 10^3 a and lower erosion rates (<100
323 mm/ka) over longer time scales of 10^3 to 10^4 a. However, this comparison between modelled erosion rates does not account
324 for the primary role that lithology has on weathering (e.g. Twidale, 1982; Ford and Williams, 1989). The sampled boulders in
325 our study were composed of Torridonian sandstone, which has been reported to undergo granular disintegration (e.g.
326 Ballantyne and Whittington, 1987), particularly around edges, and thus may have experienced higher erosion rates than the
327 crystalline rocks (e.g. gneiss, granite) used in the studies of Sohbati et al. (2018) and Lehmann et al., 2019b.



328 A major advantage of applying this new erosion-meter technique to boulders of the Beinn Alligin rock avalanche was
329 the existing constraints on Holocene erosion rates (~3.3 to 12 mm/ka) for Torridonian sandstones in NW Scotland inferred
330 from boulder edge roundness measurements (Kirkbride and Bell, 2009). The erosion rates inferred from luminescence depth
331 profiles were consistent with the estimates provided by measuring the boulder-edge roundness, when considering the differing
332 approaches and assumptions of each method. Firstly, the sampling approach for the luminescence depth profiles targeted the
333 flat-top surface of the boulders where granular disintegration would have been reduced relative to the boulder edges and
334 corners. Thus, the boulder-edge roundness based erosion rates provided an upper constraint on the long-term erosion rate
335 experienced by the boulders. Finally, the boulder-edge roundness measurements assumed steady-state erosion and could not
336 identify the potential for a transient state of erosion, whereas the approach of Lehmann et al. (2019a,b) inferred some transient
337 state of erosion (Table 3). Consequently, it is notable that the lower range of the transient erosion rates derived here using the
338 IR₅₀ (6 - 460 mm/ka), pIRIR₁₅₀ (14 - 100 mm/ka) and pIRIR₂₂₅ (11 - 180 mm/ka) signals were broadly consistent with the
339 steady-state erosion rate derived from boulder edge roundness measurements for the Torridonian sandstones (in the range of
340 ca. 3.3 to 12.0 mm/ka). Lehmann et al. (2019b) noted that their modelled steady-state erosion rates were one to two orders of
341 magnitude higher than suggested by a global compilation of bedrock surface erosion rates based on ¹⁰Be (Portenga and
342 Bierman, 2011), and measurements of upstanding, resistant lithic components (ca. 0.2 – 5.0 mm/ka) in crystalline rock surfaces
343 in Arctic Norway (André, 2002). The authors inferred that shorter-term erosion rates derived from luminescence measurements
344 were higher than the longer-term averages due to the stochastic nature of weathering impacting upon shorter-term erosion
345 rates, this is also suggested by the data presented here. These stochastic processes (i.e. varying over time) will be controlled
346 by the in-situ weathering rates, which provided the material for erosion. For bare rock surfaces in wet, temperate climates,
347 weathering rates are primarily driven by rock-type and moisture availability (i.e. precipitation) (Hall et al. 2012; Swantesson,
348 1992). The Torridonian sandstones are hard, cemented rocks (Stewart, 1984; Stewart and Donnellson, 1992) susceptible to
349 granular disintegration (e.g. Ballantyne and Whittington, 1987), which may have been stochastic in nature due to changing
350 moisture availability for chemical weathering over time (Hall et al. 2012; Swantesson, 1992). Although the Torridonian
351 sandstone is unlikely to be prone to frost shattering due to its low permeability and porosity (Lautridou, 1985; Hudec 1973 in
352 Hall et al. 2012), cracks, faults and joints in the rock may have facilitated stochastic physical weathering (Swantesson 1992;
353 Whalley et al. 1982).

354 **6.3 Late Holocene erosion history**

355 The transient state of erosion inferred by the rock luminescence measurements reflected the stochastic nature of erosion over
356 the last 4 ka, where a lower time-averaged erosion rate was interrupted by discrete intervals of higher time-averaged erosion
357 rates. Rock weathering would have been dependent upon a variety of factors, primarily rock type and climate (Merrill 1906).
358 The main constituents of the Torridonian sandstones are quartz, alkali and plagioclase feldspar (mostly albite), with
359 precipitated quartz cementing the rock being resistant to chemical weathering (Stewart and Donnellan, 1992). However, the
360 red colouring of the sandstones represents the presence of Fe within the rock (Stewart and Donnellan, 1992), which is prone



361 to chemical weathering via oxidation and reduction. Field evidence of quartz grain protrusions on the rock surfaces (Fig. 1)
362 indicated that granular disintegration, rather than flaking or shattering, was the likely weathering process that produced material
363 for erosion on these hard boulders (e.g. Swantesson, 1992). Granular disintegration has been reported as responsible for much
364 of the general microweathering in the temperate climate of Southern and Central Sweden during the Holocene (e.g.
365 Swantesson, 1992).

366 Given the coupling between precipitation, mean annual temperature and erosion (e.g. Reiners et al., 2003; Portenga
367 and Bierman, 2011), the stochastic processes producing transient erosion can relate to varying environmental conditions (Hall
368 et al. 2012; Swantesson, 1992; Whalley et al. 1982). In an environment where moisture is abundant due to high precipitation
369 rates (e.g. for NW Scotland, annual precipitation rates between 1981 and 2010 were ca. 2,300 mm/a; Met Office, 2021),
370 chemical weathering dominates, as also reported for Holocene weathering processes in Sweden (Swantesson, 1989, 1992).
371 Moisture availability, rather than temperature, is the limiting factor as studies have reported the presence of chemical
372 weathering in natural settings subject to sub-zero temperatures (e.g. northern Canada, Hall, 2007; Antarctica, Balke et al.
373 1991). Proxy evidence from across the British Isles records variability in temperature and precipitation rates over the last 4 ka,
374 where key increases in precipitation occurred at 2,750, 1,650 and 550 cal. years BP correlated to Bond cycles (Charman, 2010).
375 Thus, the transient erosion rates measured from boulders of the Beinn Alligin avalanche were potentially a representation of
376 the fluctuations in moisture availability experienced over the last 4 ka. Such processes can only be inferred from luminescence
377 depth profiles as they are sensitive to changing erosion on shorter timeframes than all other techniques.

378 **8. Conclusion**

379 This study applies the new rock luminescence techniques to a well-constrained test scenario provided by flat-topped boulders
380 from the Beinn Alligin rock avalanche in NW Scotland (a wet, temperate climate), which are lithologically consistent
381 (Torridonian sandstones), have known-age road-cuts for parameterisation of μ and $\overline{\sigma\phi_0}$, have known cosmogenic nuclide
382 exposure ages (4.22 ± 0.34 ka) and independently-derived Holocene erosion rates (ca. 3.3 to 12.0 mm/ka). Applying the rock
383 luminescence techniques for exposure dating underestimated the cosmogenic nuclide ages for the Beinn Alligin rock avalanche
384 expected due to high erosion rates (as supported by field evidence of quartz grain protrusions on the rock surfaces).
385 Alternatively, the erosion rates determined were consistent with expected rates that were independently measured in the field
386 from boulder-edge roundness when considering the relative timescales of the time-averaged erosion rates. The findings show
387 that the luminescence erosion-meter has the resolution and sensitivity required to detect transient erosion of boulders over the
388 last 4 ka reflecting the stochastic nature of erosional processes in the wet, temperate region of NW Scotland, likely in response
389 to the known fluctuations in moisture availability (and to a lesser extent temperature), which control the extent of chemical
390 weathering. This study demonstrates that the luminescence erosion-meter has huge potential for inferring erosion rates on sub-
391 millennial scales for both steady-state and transient states of erosion (i.e. stochastic processes), which is currently impossible
392 with other techniques. Larger sample populations and careful sampling of rock surfaces (avoiding the potential for rock pools
393 and trickle paths) will likely be key for accurate measurements of landscape-scale erosion, and the use of a MET-pIRIR



394 protocol (50, 150 and 225 °C) is advantageous as it can identify samples suffering from the complexities introduced by within-
395 sample variability (e.g. surficial coatings).

396

397 **Author contributions**

398 RS, DS and RSJ were involved in project conception. RS, DS, RSJ and SB performed the field sampling. RS, DS, JB and GJ
399 performed the measurements, analysis and interpretations. All authors contributed to the writing of the manuscript, including
400 the preparation of figures.

401

402 **Acknowledgments**

403 Field and laboratory work was funded by Durham University Department of Geography Research Development Fund to DS.
404 The rock luminescence equipment in the Liverpool Luminescence Laboratory was funded by a Royal Society Research Grant
405 (RG170194) to RKS. DS is supported by a NERC Independent Research Fellowship NE/T011963/1.

406

407 **References**

- 408 Aitken, M.J. 1985. Thermoluminescence dating: Past progress and future trends. *Nuclear Tracks and Radiation Measurements*,
409 10, 3-6.
- 410 André, M.-F. 2002. Rates of postglacial rock weathering of granite roches moutonnées in northern Scandinavia (Abisko-
411 Riksgränsen area, 68°N). *Geografiska Annaler* 64A, 139–150.
- 412 Balke, J., Haendel, D., Krüger, W. 1991. Contribution to the weathering-controlled removal of chemical elements from the
413 active debris layer of the Schirmacher Oasis, East Antarctica. *Zeitschrift für Geologische Wissenschaften*, 19, 153–158.
- 414 Ballantyne, C.K. 1987. The Beinn Alligin 'rock glacier'. In Ballantyne, C.K. and Sutherland, D.G., editors, *Wester Ross: field
415 guide*, Cambridge: Quaternary Research Association, 134-37.
- 416 Ballantyne, C.K. 2002. Paraglacial geomorphology. *Quaternary Science Reviews*, 21, 1935-2017.
- 417 Ballantyne, C.K. 2003. A Scottish sturzstrom: The Beinn Alligin rock avalanche, Wester Ross. *Scottish Geographical Journal*,
418 119, 159-167.
- 419 Ballantyne, C.K., Whittington, G. 1987. Niveo-aeolian sand deposits on An Teallach, Wester Ross, Scotland. *Earth and
420 Environmental Science Transactions of The Royal Society of Edinburgh*, 78, 51 – 63.
- 421 Ballantyne, C.K., Stone, J.O. 2004. The Beinn Alligin rock avalanche, NW Scotland: cosmogenic ¹⁰Be dating, interpretation
422 and significance. *The Holocene*, 14, 448-453.
- 423 Bennett, M.R., Boulton, G.S. 1993. Deglaciation of the Younger Dryas or Loch Lomond Stadial ice-field in the northern
424 Highlands, Scotland. *Journal Quaternary Science*, 8, 133–145.
- 425 Bowen, D.Q. 1992. The Pleistocene of North West Europe. *Science Progress*, 76, 209-223.
- 426 Chapot, M.S., Sohbaty, R., Murray, A.S., Pederson, J.L., Rittenour, T.M. 2012. Constraining the age of rock art by dating a
427 rockfall event using sediment and rock-surface luminescence dating techniques. *Quaternary Geochronology*, 13, 18-25.
- 428 Charman, D. 2010. Centennial climate variability in the British Isles during the mid-late Holocene. *Quaternary Science
429 Reviews*, 29, 1539-1554.
- 430 Esri. "World Imagery" [basemap]. Scale Not Given. "World Imagery". December 12, 2009.
431 https://services.arcgisonline.com/ArcGIS/rest/services/World_Imagery/MapServer. (Feb, 11, 2021).
- 432 Esri. "Topographic" [basemap]. Scale Not Given. "World Topographic Map". June 14, 2013.
433 <http://www.arcgis.com/home/item.html?id=30e5fe3149c34df1ba922e6f5bbf808f>. (Feb, 11, 2021).
- 434 Ford, D., Williams, P. 1989. *Karst Geomorphology and Hydrology*. Unwin Hyman, London. 601 pp.
- 435 Gliganic, L.A., Meyer, M.C., Sohbaty, R., Jain, M., Barrett, S. 2019. OSL surface exposure dating of a lithic quarry in Tibet:
436 Laboratory validation and application. *Quaternary Geochronology*, 49, 199-204.



- 437 Golledge, N.R., Hubbard, A., Sugden, D.E. 2008. High-resolution numerical simulation of Younger Dryas glaciation in
438 Scotland. *Quaternary Science Reviews*, 27, 888-904.
- 439 Gordon, J.E. 1993. Beinn Alligin. In Gordon, J.E. and Sutherland, D.G., editors *Quaternary of Scotland*, London: Chapman
440 and Hall, 118-22.
- 441 Habermann, J., Schilles, T., Kalchgruber, R., Wagner, G.A., 2000. Steps towards surface dating using luminescence. *Radiation*
442 *Measurements* 32, 847-851.
- 443 Hall, K. 2007. Evidence for freeze-thaw events and their implications for rock weathering in northern Canada, II: the
444 temperature at which water freezes in rock. *Earth Surface Processes and Landforms*, 32, 249–259.
- 445 Hall, K., Arocena, J.M., Boelhouwers, J., Zhu, L. 2005. The influence of aspect on the biological weathering of granites:
446 observations from the Kunlun Mountains, China. *Geomorphology*, 67, 171–188.
- 447 Hall, K., Guglielmin, M., Strini, A. 2008. Weathering of granite in Antarctica II: thermal data at the grain scale. *Earth Surface*
448 *Processes and Landforms*, 33, 475–493.
- 449 Hall, K., Thorn, C., Sumner, P. 2012. On the persistence of ‘weathering’. *Geomorphology*, 149-150, 1-10.
- 450 Hanna, F.K. 1966. A technique for measuring the rate of erosion of cave passages. *Proceedings University of Bristol*
451 *Speleology Society*, 11, 83–86.
- 452 Herman, F., Rhodes, E.J., Braun, J., Heiniger, L. 2010. Uniform erosion rates and relief amplitude during glacial cycles in the
453 Southern Alps of New Zealand, as revealed from OSL-thermochronology. *Earth and Planetary Science Letters*, 297, 183-
454 189.
- 455 High, C.J., Hanna, F.K. 1970. A method for the direct measurement of erosion on rock surfaces. *British Geomorphological*
456 *Research Group Technical Bulletin*, 5, 1–25.
- 457 Hijmans, R.J. (2019). raster: Geographic Data Analysis and Modeling. R package version 2.9-23. [https://CRAN.R-](https://CRAN.R-project.org/package=raster)
458 [project.org/package=raster](https://CRAN.R-project.org/package=raster)
- 459 Huntley, D.J., Lamothe, M. 2001. Ubiquity of anomalous fading in K-feldspars and the measurement and correction for it in
460 optical dating, 38, 1093-1106.
- 461 Israelli, Y., Emmanuel, S. 2018. Impact of grain size and rock composition on simulated rock weathering. *Earth Surface*
462 *Dynamics*, 6, 319-327.
- 463 Jenkins, G. T. H., Duller, G. A. T., Roberts, H. M., Chiverrell, R. C., Glasser, N. F. 2018. A new approach for luminescence
464 dating glaciofluvial deposits – High precision optical dating of cobbles. *Quaternary Science Reviews*, 192, 263 – 273.
- 465 Kirkbride, M.P., Bell, C.M. 2010. Edge-roundness of boulders of Torridonian Sandstone (northwest Scotland): applications
466 for relative dating and implications for warm and cold climate weathering rates. *Boreas* DOI 10.1111/j.1502-
467 3885.2009.00131.
- 468 Kolb, T., Fuchs, M. 2018. Luminescence dating of pre-Eemian (pre-MIS 5e) fluvial terraces in Northern Bavaria (Germany)
469 – Benefits and limitations of applying a pIRIR225-approach. *Geomorphology*, 321, 16-32.
- 470 Laskaris, N., Liritzis, I. 2011. A new mathematical approximation of sunlight penetrations in rocks for surface luminescence
471 dating. *Journal of Luminescence*, 131, 1874-1884.
- 472 Lehmann, B., Valla, P.G., King, G.E., Herman, F. 2018. Investigation of OSL surface exposure dating to reconstruct post-LIA
473 glacier fluctuations in the French Alps (Mer de Glace, Mont Blanc massif). *Quaternary Geochronology*, 44, 63-74.
- 474 Lehmann, B., Herman, F., Valla, P.G., King, G.E., Biswas, R.H. 2019a. Evaluating post-glacial bedrock erosion and surface
475 exposure duration by coupling in situ optically stimulated luminescence and 10Be dating. *Earth Surface Dynamics*, 7, 633-
476 662.
- 477 Lehmann, B., Herman, F., Valla, P.G., King, G.E., Biswas, R.H., Ivy-Ochs, S., Steinemann, O., Christl, M. 2019b. Postglacial
478 erosion of bedrock surfaces and deglaciation timing: New insights from the Mont Blanc massif (western Alps). *Geology*,
479 <https://doi.org/10.1130/G46585.1>
- 480 Li, B., Li, S-H. 2011. Luminescence dating of K-feldspar from sediments: A protocol without anomalous fading correction.
481 *Quaternary Geochronology*. 6, 468-479.
- 482 Liu, J., Murray, A., Sohbat, R., Jain, M. 2016. The effect of test dose and first IR Stimulation temperature on post-IR IRSL
483 measurements of rock slices. *Geochronometria*, 43, 179-187.
- 484 Luo, M., Chen, J., Liu, J., Qin, J., Owen, L., Han, F., Yang, H., Wang, H., Zhang, B., Yin, J., Li, Y. 2018. A test of rock surface
485 luminescence dating using glaciofluvial boulders from the Chinese Pamir. *Radiation Measurements*, 120, 290-297.
- 486 Merrill, G.P. 1906. *A Treatise on Rocks. Rock-Weathering and Soils*, Macmillan, New York. 400 pp.



- 487 Met Office, 2021. UK Climate averages (1981-2010): Kinlochewe Met station (57.613°N, -5.308°W)
488 <https://www.metoffice.gov.uk/research/climate/maps-and-data/uk-climate-averages/gfhpz0nu4> [Accessed 18/01/2021].
- 489 Meyer, M.C., Gliganic, L.A., Jain, M., Schmidmair, D. 2018. Lithological controls on light penetration into rock surfaces –
490 Implications for OSL and IRSL surface exposure dating. *Radiation Measurements*, 120, 298-304.
- 491 Ou, X.J., Roberts, H.M., Duller, G.A.T., Gunn, M.D., Perkins, W.T. 2018. Attenuation of light in different rock types and
492 implications for rock surface luminescence dating. *Radiation Measurements*, 120, 305-311.
- 493 Parish, R. 1994. The influence of feldspar weathering on luminescence signals and the implications for luminescence dating
494 of sediments. In Robinson, D.A. and Williams, R.B.G., editors, *Rock weathering and landform
495 evolution*, Chichester: Wiley.
- 496 Pederson, J.L., Chapot, M.S., Simms, S.R., Sohbaty, R., Rittenour, T.M., Murray, A.S., Cox, G. 2014. Age of Barrier Canyon-
497 style rock art constrained by cross-cutting relations and luminescence dating techniques. *PNAS* 111, 12986-12991.
- 498 Polikreti, K., Michael, C.T., Maniatis, Y., 2002. Authenticating marble sculpture with thermoluminescence. *Ancient TL* 20,
499 11-18.
- 500 Polikreti, K. Michael, C.T. and Maniatis, Y. 2003. Thermoluminescence characteristics of marble and dating of freshly
501 excavated marble objects. *Radiation Measurements*, 37, 87–94.
- 502 Portenga, E.W., Bierman, P.R. 2011. Understanding Earth’s eroding surface with ¹⁰Be. *GSA Today*, 21, 4-10.
- 503 Prescott, J.R., Hutton, J.T. 1994. Cosmic ray and gamma ray dosimetry for TL and ESR. *Nuclear Tracks and Radiation
504 Measurements*, 14, 223-227.
- 505 Reiners, P.W., Brandon, M.T. 2006. Using thermochronology to understand orogenic erosion. *Annual Review of Earth
506 Planetary Science*, doi: 10.1146/annurev.earth.34.031405.125202.
- 507 Riebe CS, Kirchner JW, Finkel RC. 2003. Long-term rates of weathering and physical erosion from cosmogenic nuclides and
508 geochemical mass balance. *Geochim. Cosmochim. Acta*, 67, 4411–27
- 509 Roberts, H.M. 2012. Testing Post-IR IRSL protocols for minimising fading in feldspars, using Alaskan loess with independent
510 chronological control. *Radiation Measurements*, 47, 716-724.
- 511 Robinson, D.A., Williams, R.B.G. 1987. Surface crusting of sandstones in southern England and northern France. In: Gardner,
512 V. (Ed.), *International Geomorphology 1986*, vol. 2. Wiley, Chichester, pp. 623–635.
- 513 Singhvi, A.K., Deraniyagala, S.U., Sengupta, D. 1986. Thermoluminescence dating of Quaternary red-sand beds: a case study
514 of coastal dunes in Sri Lanka. *Earth and Planetary Science Letters*, 80, 139-144.
- 515 Sissons, J.B. 1975. A fossil rock glacier in Wester Ross. *Scottish Journal of Geology*, 11, 83-86.
- 516 Sissons, J.B. 1976. A fossil rock glacier in Wester Ross. Reply to W.B. Whalley. *Scottish Journal of Geology*, 12, 178-79.
- 517 Smedley, R.K., Duller, G.A.T., Roberts, H.M. 2015. Assessing the bleaching potential of the post-IR IRSL signal for individual
518 K-feldspar grains: implications for single-grain dating. *Radiation Measurements*, 79, 33 – 42.
- 519 Smedley, R.K., Glasser, N.F., Duller, G.A.T. 2016. Luminescence dating of glacial advances at Lago Buenos Aires (~46 °S),
520 Patagonia. *Quaternary Science Reviews*, 134, 59 – 73.
- 521 Sohbaty, R., Murray, A.S., Jain, M., Buylaert, J.P., Thomsen, K.J. 2011. Investigating the resetting of OSL signals in rock
522 surfaces. *Geochronometria*, 38, 249–258.
- 523 Sohbaty, R., Murray, A.S., Buylaert, J.P., Almeida, N.A.C., Cunha, P.P. 2012a. Optically stimulated luminescence (OSL)
524 dating of quartzite cobbles from the Tapada do Montinho archaeological site (east-central Portugal). *Boreas*, 41, 452–462.
- 525 Sohbaty, R., Murray, A.S., Chapot, M.S., Jain, M., Pederson, J., 2012b. Optically stimulated luminescence (OSL) as a
526 chronometer for surface exposure dating. *Journal of Geophysical Research Solid Earth*, 117.
- 527 Sohbaty, R., Liu, J., Jain, M., Murray, A.S., Egholm, D., Pairs, R., Guralnick, B. 2018. Centennial- to millennial-scale hard
528 rock erosion rates deduced from luminescence-depth profiles. *Earth and Planetary Science Letter*, 493, 218-230.
- 529 Stewart, A.D. 1982. Late Proterozoic rifting in NW Scotland: the genesis of the ‘Torridonian’. *Journal of Geological Society
530 of London*, 139, 413-420.
- 531 Stewart, A.D. Donnellson, N.C.B. 1992. Geochemistry and provenance of red sandstones in the Upper Proterozoic Torridon
532 Group in Scotland. *Scottish Journal of Geology*, 28, 143-153.
- 533 Stocker, T.F., D. Qin, G.-K. Plattner, L.V. Alexander, S.K. Allen, N.L. Bindoff, F.-M. Bréon, J.A. Church, U. Cubasch, S.
534 Emori, P. Forster, P. Friedlingstein, N. Gillett, J.M. Gregory, D.L. Hartmann, E. Jansen, B. Kirtman, R. Knutti, K. Krishna
535 Kumar, P. Lemke, J. Marotzke, V. Masson-Delmotte, G.A. Meehl, I.I. Mokhov, S. Piao, V. Ramaswamy, D. Randall, M.
536 Rhein, M. Rojas, C. Sabine, D. Shindell, L.D. Talley, D.G. Vaughan and S.-P. Xie, 2013: Technical Summary. In: *Climate*

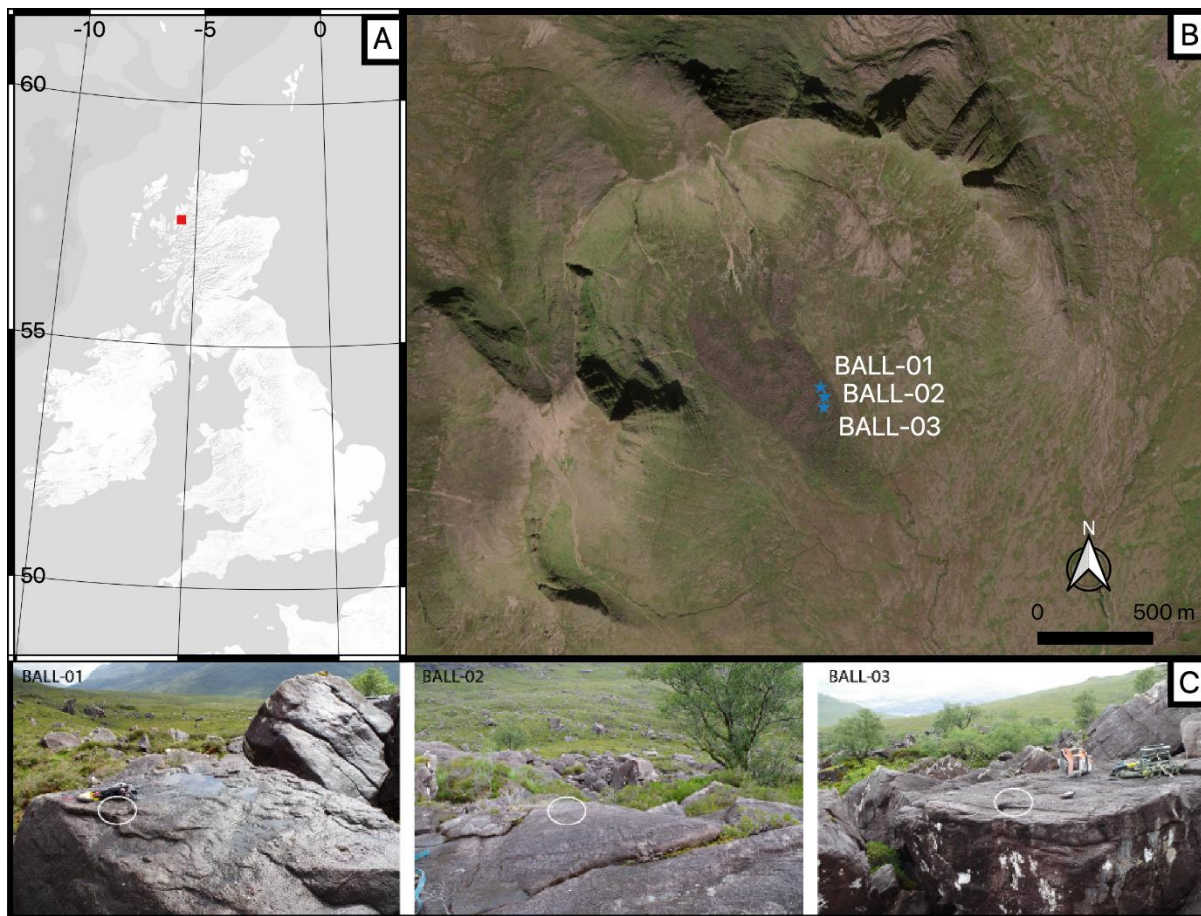


- 537 Change 2013: The Physical Science Basis. Contribution of Working Group I to the Fifth Assessment Report of the
538 Intergovernmental Panel on Climate Change [Stocker, T.F., D. Qin, G.-K. Plattner, M. Tignor, S.K. Allen, J. Boschung,
539 A. Nauels, Y. Xia, V. Bex and P.M. Midgley (eds.)]. Cambridge University Press, Cambridge, United Kingdom and New
540 York, NY, USA.
- 541 Swantesson, J.O.H. 1989. Weathering phenomena in a cool temperate climate. Göteborgs University, Naturgeogr. Inst., Guni.
542 Rapport, 28.
- 543 Swantesson, J.O.H. 1992. Recent microweathering phenomena in Southern and Central Sweden. Permafrost and Periglacial
544 Processes, 3, 275-292.
- 545 Swantesson, J.O.H., Moses, C.A., Berg, G.E., Jansson, K.M. 2006. Methods for measuring shore platform micro-erosion: a
546 comparison of the micro-erosion meter and laser scanner. *Z. Geomorphology*, 144, 1–17.
- 547 Thomsen, K. J., Murray, A. S., Jain, M. and Bøtter-Jensen, L. 2008. Laboratory fading rates of various luminescence signals
548 from feldspar-rich sediment extracts. *Radiation Measurements*, 43, 1474 –1486.
- 549 Thomsen, K.J., Murray, A.S., Jain, M. 2011. Stability of IRSL signals from sedimentary K-feldspar samples. *Geochronometria*,
550 38, 1-13.
- 551 Thomsen, K.J., Kook, M., Murray, A.S., Jain, M. 2018. Resolving luminescence in spatial and compositional domains.
552 *Radiation Measurements*, 15, 260-266.
- 553 Thorn, C.E., Darmody, R.G., Dixon, J.C., Schlyter, P. 2001. The chemical weathering regime of Kärkevage, arctic-alpine
554 Sweden. *Geomorphology*, 41, 37–52.
- 555 Trauerstein, M., Lowick, S.E., Preusser, F., Schlunegger, F. 2014. Small aliquot and single grain IRSL and post-IR IRSL
556 dating of fluvial and alluvial sediments from the Pativilca valley, Peru. *Quaternary Geochronology*, 22, 163-174.
- 557 Trudgill, S.T., Viles, H., Inkpen, R.J., Cooke, R.U. 1989. Remeasurement of weathering rates, St. Paul's Cathedral, London.
558 *Earth Surface Processes and Landforms*, 14, 175–196.
- 559 Twidale, C.R., 1982. *Granite Landforms*. Elsevier, Amsterdam. 372 pp.
- 560 Vafiadou, A., Murray, A.S., Liritzis, I., 2007. Optically stimulated luminescence (OSL) dating investigations of rock and
561 underlying soil from three case studies. *Journal of Archaeological Science* 34, 1659-1669.

563

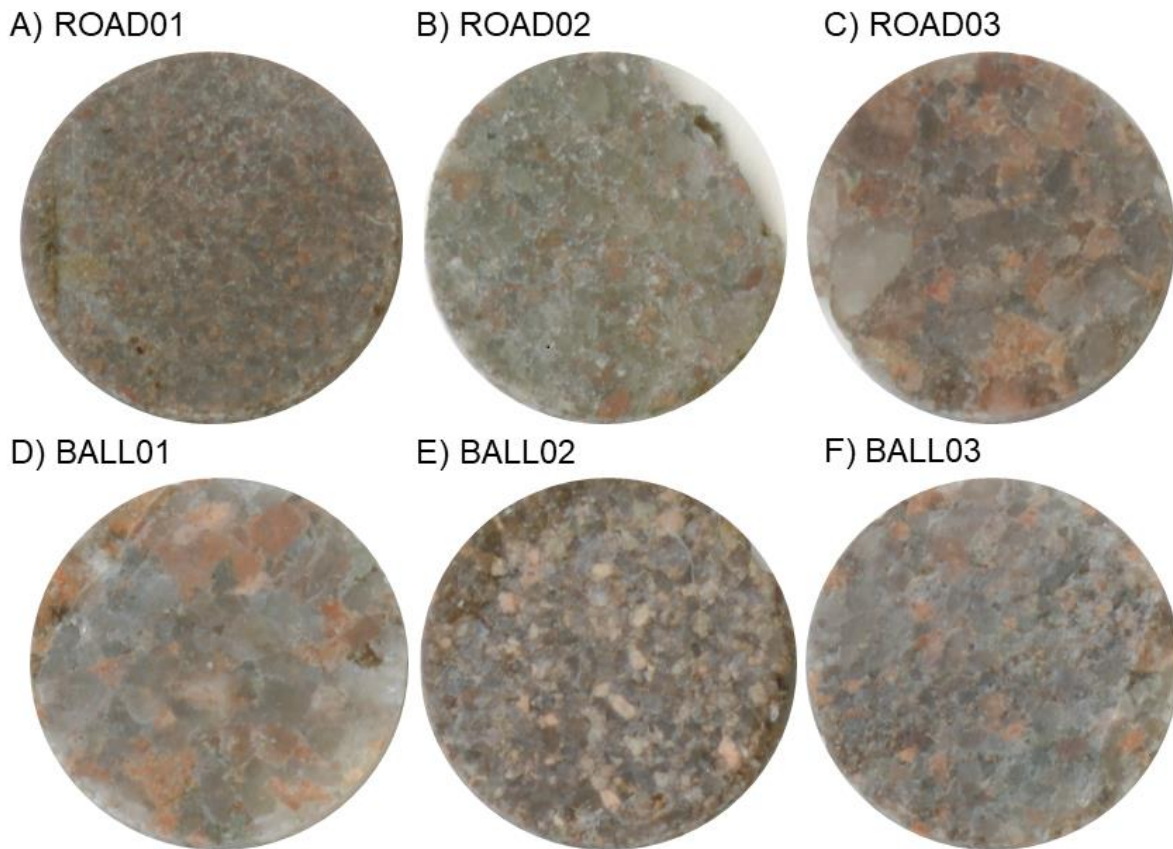
564

565



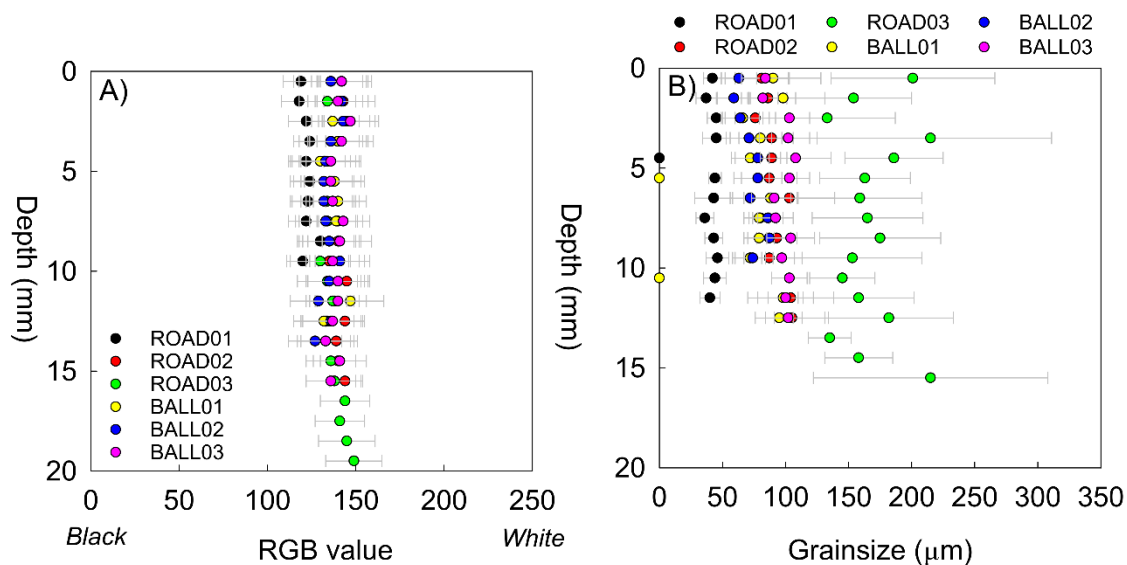
566
567
568
569
570

Figure 1. Location of the Beinn Alligin rock avalanche ($57^{\circ}35'N$, $05^{\circ}34'W$) in NW Scotland (A) and sample sites on the rock avalanche deposit (B). The backgrounds used are ESRI World Terrain Base (A) and ESRI World Imagery (B). Photographs of flat-topped boulders sampled for BALL01, BALL02 and BALL03 (C).



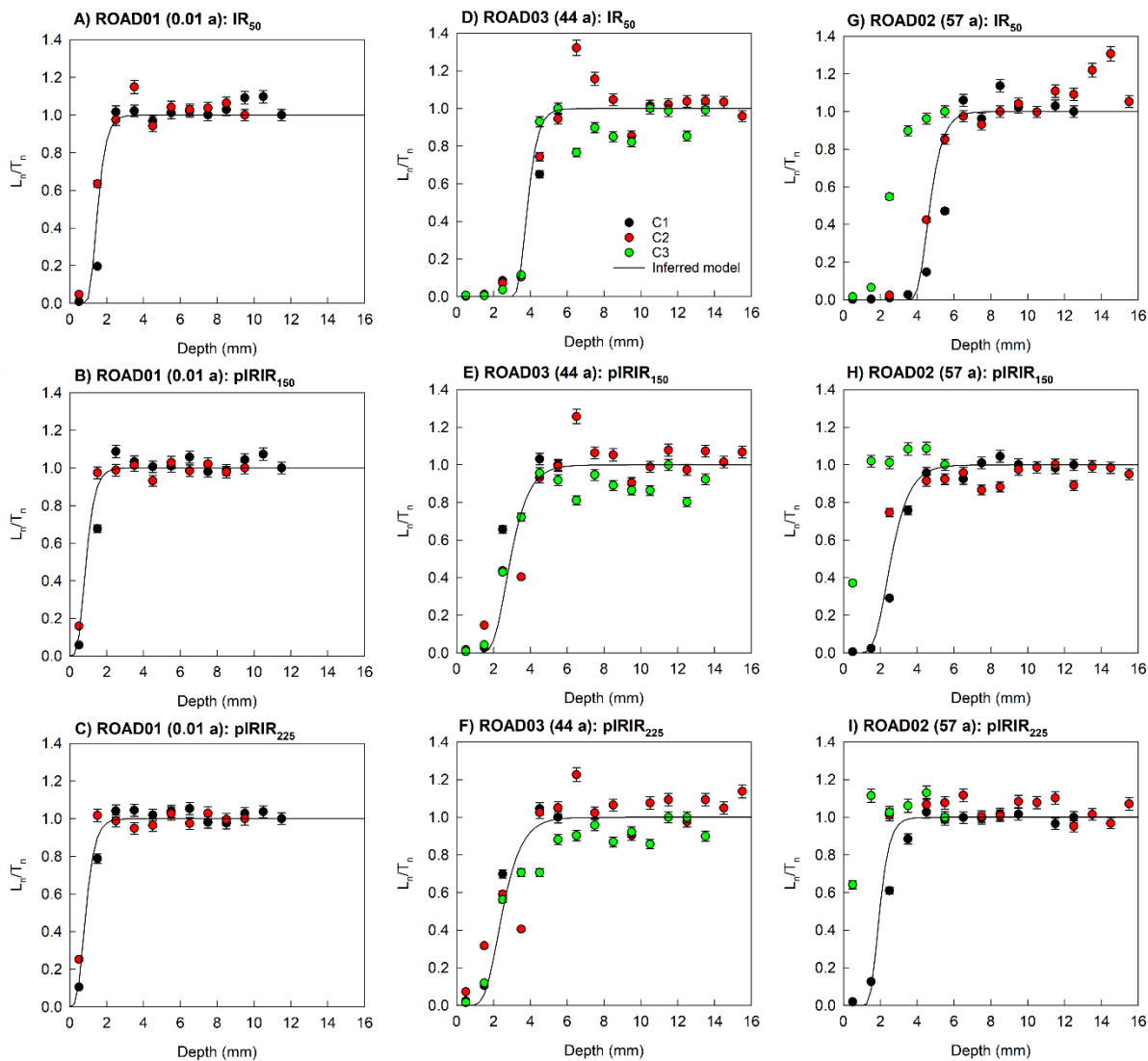
571
572
573

Figure 2. Images of example rock slices (0.7 mm diameter) for each sample taken using the EPSON Expression 11000XL flatbed scanner.



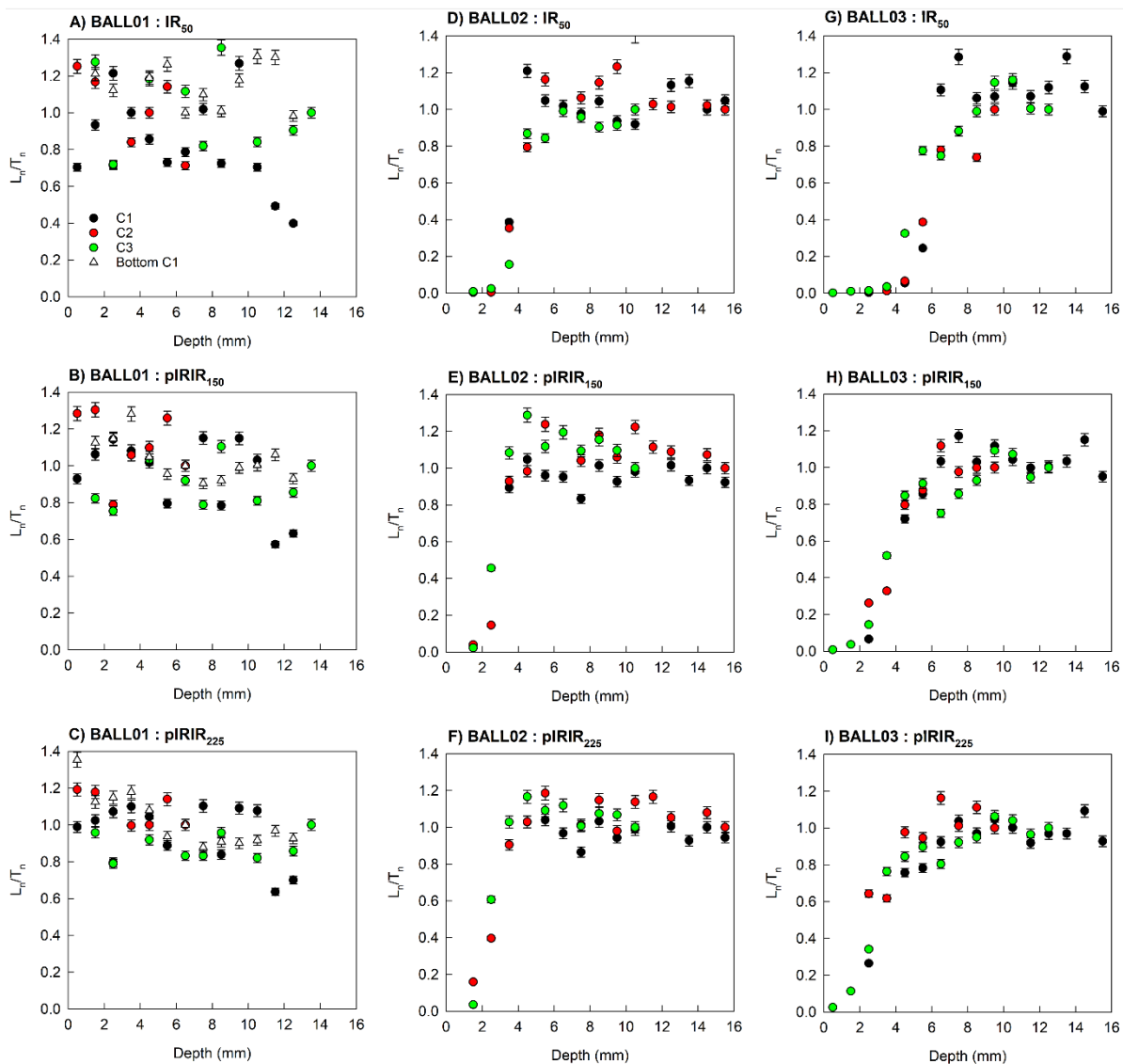
574
575
576

Figure 3. (A) RGB values (0 = black and 255 = white) and (B) grainsize for each sample, calculated as the mean (\pm standard deviation) of the slices at each depth in all of the replicate cores analysed.



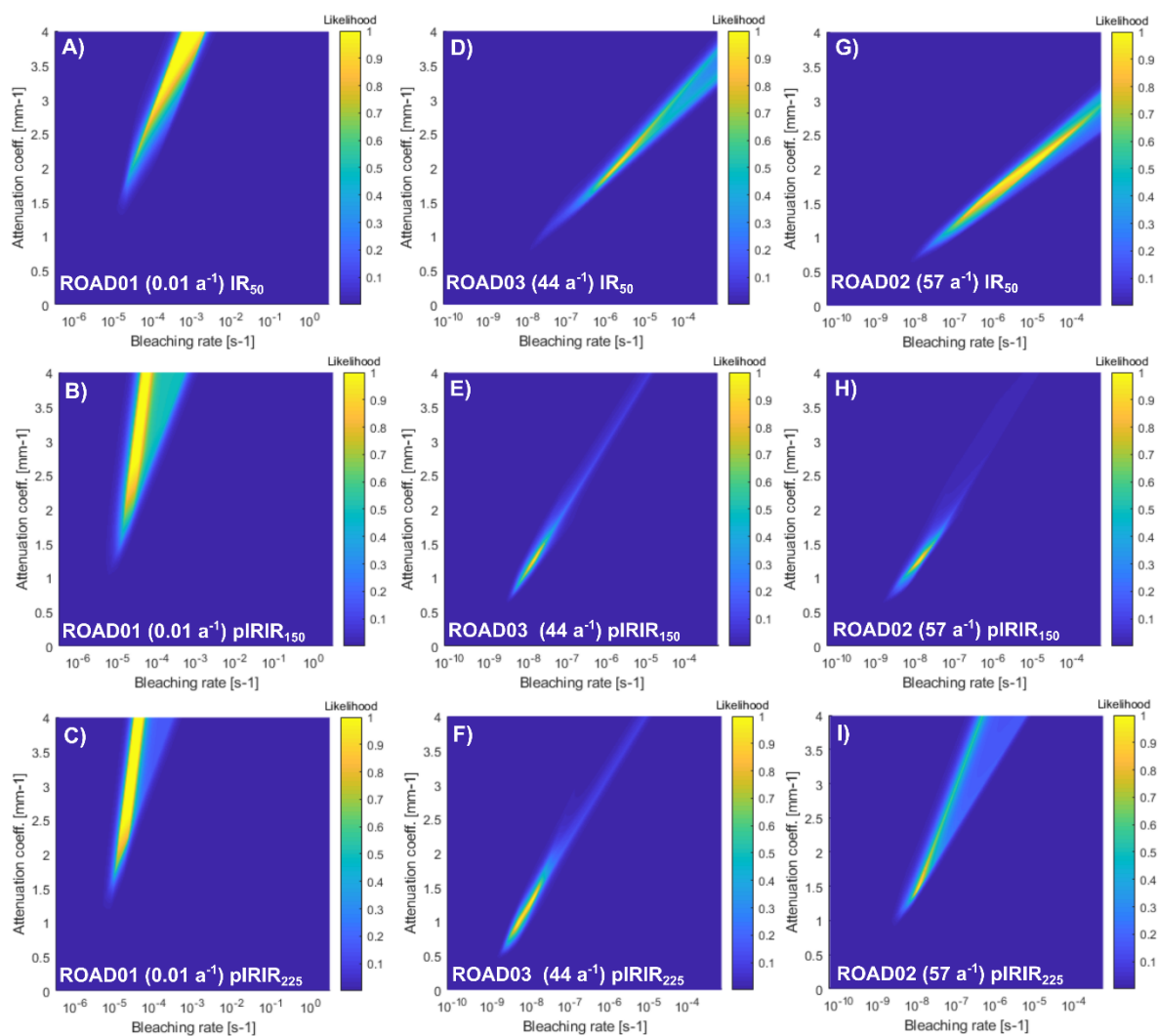
577
578
579
580

Figure 4. Presented in age-order are the IRSL-depth profiles for each replicate cores analysed using the IR₅₀ (A,D,G), pIRIR₁₅₀ (B,E,H) and pIRIR₂₂₅ (C,F,I) signals for samples ROAD01 (0.01 a; A-C), ROAD03 (44 a; D-F) and ROAD02 (57 a; G-I).

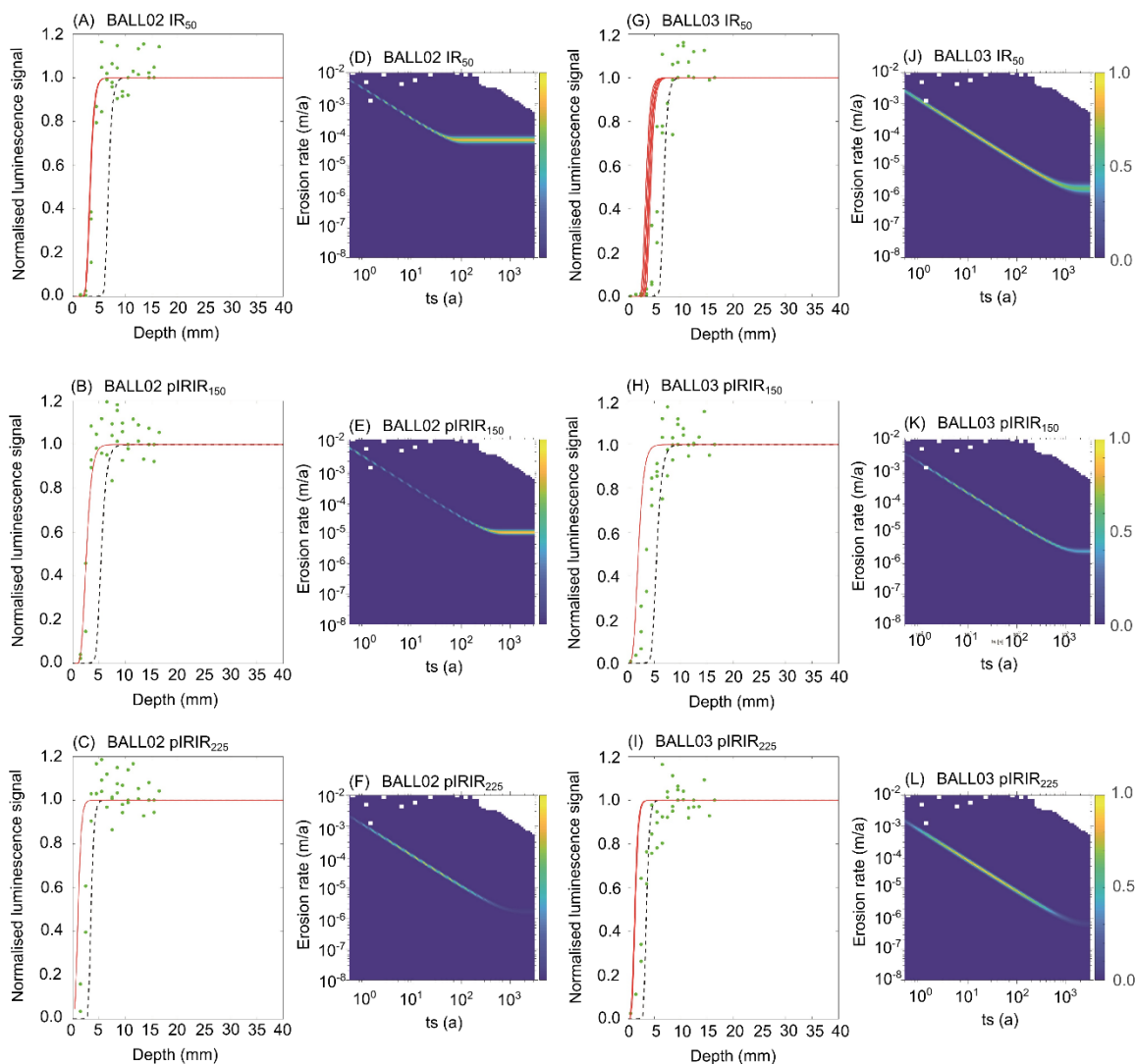


581
582
583

Figure 5. IRSL-depth profiles for each replicate cores analysed using the IR₅₀ (A,D,G), pIRIR₁₅₀ (B,E,H) and pIRIR₂₂₅ (C,F,I) signals for samples BALL01 (A-C), BALL02 (D-F) and BALL03 (G-I).



584
 585 **Figure 6.** Presented in age-order is the relationship between $\overline{\sigma\phi_0}$ and μ parameters for ROAD01 (A-C), ROAD03 (D-F) and
 586 ROAD02 (G-I) using the IR₅₀ (A,D,G), pIRIR₁₅₀ (B,E,H) and pIRIR₂₂₅ (C,F,I) signals using the approach of Lehmann et al. (2018).
 587
 588



589
 590
 591
 592
 593
 594
 595

Figure 7. Luminescence depth profiles and inversion results (using the approach of Lehmann et al. 2019a) for samples BALL02 (A-F) and BALL03 (G-L) using the IR₅₀ (A,D,G,J), pIRIR₁₅₀ (B,E,H,K) and pIRIR₂₂₅ (C,F,I,L) signals. Dashed black lines show reference profiles, taking terrestrial cosmogenic nuclide (TCN) exposure age with no erosion correction (t_0); red lines represent inferred fits where likelihood is >0.95. Probability distributions inverted from the respective plots of luminescence depth profiles are also shown. Forbidden zones define the range of solutions with high erosion rates and durations that are not feasible within the bounds of the ¹⁰Be and luminescence data.



Table 1. Luminescence results for the rock slices analysed in this study. Environmental dose-rates were determined using high-resolution gamma spectrometry. The dose-rates were calculated using the conversion factors of Guerin et al. (2011) and alpha (Bell, 1980) and beta (Guerin et al. 2012) dose-rate attenuation factors. An internal K-content of $10 \pm 2\%$ (Smedley et al. 2012) and internal U and Th concentrations of 0.3 ± 0.1 ppm and 1.7 ± 0.4 ppm (Smedley and Pearce, 2016) were used to determine the internal alpha and beta dose-rates. An α -value of 0.10 ± 0.02 (Balescu and Lamothe, 1993) was used to calculate the alpha dose-rates. Cosmic dose-rates were determined after Prescott and Hutton (1994). Dose-rates were calculated using the Dose Rate and Age Calculator (DRAC; Durcan et al. 2015). Grain size was measured by randomly selecting grains in the rock slices for each sample and calculating ± 1 standard deviation around the mean grain size.

Sample	Grain size (μm)	U (ppm)	Th (ppm)	K (%)	Internal alpha dose- rate (Gy/ka)	Internal beta dose- rate (Gy/ka)	Internal alpha dose- rate (Gy/ka)	External beta dose- rate (Gy/ka)	External gamma dose-rate (Gy/ka)	External cosmic dose-rate (Gy/ka)	Total dose- rate (Gy/ka)
BALL02	56-91	1.02 \pm 0.15	4.85 \pm 0.28	1.73 \pm 0.29	0.14 \pm 0.04	0.27 \pm 0.06	0.21 \pm 0.05	1.62 \pm 0.00	0.78 \pm 0.08	0.31 \pm 0.03	3.32 \pm 0.12
BALL03	79-117	1.02 \pm 0.14	5.21 \pm 0.28	1.86 \pm 0.29	0.16 \pm 0.04	0.35 \pm 0.08	0.17 \pm 0.04	1.71 \pm 0.00	0.83 \pm 0.08	0.31 \pm 0.03	3.52 \pm 0.12
ROAD01	33-51	2.07 \pm 0.27	7.80 \pm 0.42	2.45 \pm 0.43	0.10 \pm 0.03	0.16 \pm 0.03	0.61 \pm 0.12	2.43 \pm 0.00	1.22 \pm 0.11	0.30 \pm 0.03	4.81 \pm 0.18
ROAD02	67-113	1.55 \pm 0.18	5.67 \pm 0.38	2.88 \pm 0.40	0.15 \pm 0.04	0.32 \pm 0.08	0.23 \pm 0.05	2.59 \pm 0.00	1.16 \pm 0.10	0.30 \pm 0.03	4.76 \pm 0.15
ROAD03	112-225	1.93 \pm 0.21	5.30 \pm 0.30	1.96 \pm 0.31	0.18 \pm 0.04	0.58 \pm 0.20	0.14 \pm 0.04	1.85 \pm 0.00	0.96 \pm 0.08	0.29 \pm 0.03	4.00 \pm 0.22



605

610

Table 2. Calibration factors determined by fitting depth profiles. Note that values presented are medians.

Sample	IRSL signal	$\overline{\sigma\phi_0}$ (s ⁻¹)	Range $\pm 1 \sigma$ (s ⁻¹)	μ (mm ⁻¹)	Range $\pm 1 \sigma$ (mm ⁻¹)
ROAD01	IR ₅₀	2.80e ⁻⁴	8.41e ⁻⁴ – 6.43e ⁻⁵	3.2	2.5 – 3.8
	pIRIR ₁₅₀	3.27e ⁻⁵	1.16e ⁻⁴ – 2.14e ⁻⁵	3.1	2.2 – 3.7
	pIRIR ₂₂₅	2.88e ⁻⁵	3.99e ⁻⁵ – 1.51e ⁻⁵	3.0	2.3 – 3.6
ROAD02	IR ₅₀	6.67e ⁻⁶	1.27e ⁻⁴ – 3.50e ⁻⁷	2.1	1.4 – 2.6
	pIRIR ₁₅₀	1.73e ⁻⁸	9.64e ⁻⁸ – 9.75e ⁻⁹	1.5	1.1 – 2.3
	pIRIR ₂₂₅	9.01e ⁻⁸	5.53e ⁻⁷ – 2.31e ⁻⁸	2.8	1.8 – 3.6
ROAD03	IR ₅₀	1.56e ⁻⁵	1.64e ⁻⁴ – 1.48e ⁻⁶	2.7	2.0 – 3.2
	pIRIR ₁₅₀	3.80e ⁻⁸	4.40e ⁻⁷ – 1.12e ⁻⁸	1.5	1.1 – 2.5
	pIRIR ₂₂₅	1.70e ⁻⁸	1.17e ⁻⁷ – 4.70e ⁻⁹	1.4	0.9 – 2.5

615

620



Table 3. Luminescence exposure ages and erosion rates determined using the approach of Lehmann et al. (2018) and Lehmann et al. (2019a), respectively. The values of $\overline{\sigma\phi_0}$ and μ were determined from known-age sample ROAD02 (57 a).

Sample	Signal	$\overline{\sigma\phi_0}$ (s ⁻¹)	μ (mm ⁻¹)	\dot{D} (Gy/ka)	D_0 (Gy)	Exposure age (a)	Steady-state erosion rate (mm/ka)	Min. initiation time (a)	Max. transient erosion rate (mm/ka)	Initiation time (a)	Min. transient erosion rate (mm/ka)	Initiation time (a)
BALL02	IR ₅₀	$6.67e^6$	2.1	3.32 ± 0.12	500	8.0 ± 1.5	66	73	-	-	-	-
	pIRIR ₁₅₀	$1.73e^8$	1.5	3.32 ± 0.12	350	66 ± 16	9	593	-	-	-	-
	pIRIR ₂₂₅	$9.01e^8$	2.8	3.32 ± 0.12	350	263 ± 30	-	-	310	4	12	90
BALL03	IR ₅₀	$6.67e^6$	2.1	3.52 ± 0.12	500	387 ± 103	-	-	460	3	6	231
	pIRIR ₁₅₀	$1.73e^8$	1.5	3.52 ± 0.12	350	296 ± 54	-	-	100	19	14	137
	pIRIR ₂₂₅	$9.01e^8$	2.8	3.52 ± 0.12	350	362 ± 49	-	-	180	4	11	73